Monthly Notices of the ROYAL ASTRONOMICAL SOCIETY

MNRAS **525,** 150–163 (2023) https://doi.org/10.1093/mnras/stad2265
Advance Access publication 2023 July 27

Shallow-water modelling of the atmospheric circulation regimes of brown dwarfs and their observable features

Mark Hammond [1,2]★ Nathan J. Mayne,[3] William J. M. Seviour,[4] Neil T. Lewis,[1,4] Xianyu Tan[1,5,6] and Dann Mitchell[2]

[1]*Atmospheric, Oceanic and Planetary Physics, Department of Physics, University of Oxford, Oxford OX1 3PU, UK*
[2]*School of Geographical Sciences, University of Bristol, Bristol BS8 1SS, UK*
[3]*Department of Physics and Astronomy, University of Exeter, Exeter, EX4 4QL, UK*
[4]*Department of Mathematics and Statistics, Univearsity of Exeter, Exeter, EX4 4QF, UK*
[5]*Tsung-Dao Lee Institute, Shanghai Jiao Tong University, 520 Shengrong Road, Shanghai, People's Republic of China*
[6]*School of Physics and Astronomy, Shanghai Jiao Tong University, 800 Dongchuan Road, Shanghai, People's Republic of China*

Accepted 2023 July 18. Received 2023 June 14; in original form 2022 October 28

ABSTRACT

Observations of time-varying thermal emission from brown dwarfs suggest that they have large-scale atmospheric circulation. The magnitude of this variability ranges from a few per cent to tens of per cent, implying a range of sizes of atmospheric perturbations. Periodograms of phase curves of the thermal emission reveal a range of peaks with different periods and widths, suggesting different atmospheric flow speeds and directions. This implies a variety of atmospheric circulations in the different brown dwarfs observed to date, but there is no general theoretical understanding of the circulation regimes these objects can support, and the resulting sizes and velocities of their atmospheric features. We therefore use an idealized 2D shallow-water model of a brown dwarf atmosphere to understand their potential large-scale circulation regimes. We non-dimensionalize the model to reduce the number of input parameters to two non-dimensional numbers: the thermal Rossby number and the non-dimensional radiative time-scale. This allows us to define a parameter space that bounds the entire range of brown dwarf behaviour possible in our model. We analyse the resulting height, velocity, and potential vorticity fields in this parameter space, and simulate observed phase curve and periodograms for comparison with real observations. We use our results to qualitatively define four circulation regimes, which we hope will be useful for interpreting observations and for guiding simulations with more detailed physical models.

Key words: brown dwarfs – methods: numerical.

1 INTRODUCTION

The study of brown dwarfs has drawn a link between gaseous planets and stars. Brown dwarfs are objects composed of hydrogen with masses similar to or greater than giant planets, and less than stars. They are thought to form in the way as stars, but do not have enough mass for fusion to occur (Burrows et al. 2001). Their atmospheres appear more similar to giant planets than stars, and observations suggest that they have jets and surface features similar to giant planets in our Solar system (Showman, Tan & Parmentier 2020). They are self-luminous and have larger radii than most exoplanets so are excellent targets for atmospheric observations.

Time-resolved observations have revealed variations in their emitted flux, typically of a few per cent but reaching up to tens of per cent (Robinson & Marley 2014; Artigau 2018; Zhou et al. 2022). Vos et al. (2022) found that photometric variability is particularly common in young brown dwarfs in the L2–T4 range. This compares to variability of a few per cent in optical emission for Jupiter and Neptune as point sources, and tens of per cent for Jupiter in the infrared (Artigau 2018). Idealized atmospheric models of brown dwarf atmospheres have produced similar variability to that simulated for Jupiter (Showman 2007; Zhang & Showman 2014). Variability is a key process in the atmosphere of the gas giants of the Solar system, so it may also be a key observational window into the atmospheric properties of brown dwarfs.

In this study, we simulate a suite of idealized models of brown dwarf atmospheres, using a 2D 'shallow-water' model forced by random perturbations. We aim to identify circulation regimes in the entire parameter space of potential brown dwarf atmospheres, and to link these directly to observable variability. Previous studies of brown dwarf atmospheres used similar shallow-water models (Zhang & Showman 2014) or 3D General Circulation Models (GCMs; Tan & Showman 2021a, b; Tan 2022). Both types of model have been extensively used with a range of complexities to model gaseous exoplanets (Showman & Polvani 2011; Showman, Lewis & Fortney 2015). We chose the simple and computationally efficient shallow-water model to investigate a large parameter space, to focus on the overall dynamical regimes of the atmosphere rather than its complex 3D behaviour, and to run models with high spatial and time resolution.

We build on the approach of Zhang & Showman (2014) by non-dimensionalizing the shallow-water model so that our results encompass its entire range of plausible behaviour. The 2D shallow-

★ E-mail: mark.hammond@physics.ox.ac.uk

water model has multiple parameters (radius, rotation rate, etc.), making it difficult to simulate and understand the circulation regimes in the resulting multidimensional parameter space. We therefore non-dimensionalize our model so that it only depends on two parameters: the thermal Rossby number and the non-dimensional radiative time-scale (Wang et al. 2018). The non-dimensional model results are identical for any simulations with the same non-dimensional parameters. This allows us to identify circulation regimes of the entire 2D parameter space which encompasses all of the possible model results, up to constants of proportionality. We define plausible ranges of each non-dimensional parameter based on the properties of real brown dwarfs.

In Section 2, we review relevant work on brown dwarfs, focusing on observations and simulations of variability. Section 3 describes the shallow-water model that we use to simulate a suite of brown dwarf atmospheres. We present the results from this model in Sections 4 and 5, plotting atmospheric properties and simulated observations for the whole parameter space. Section 6 discusses the circulation regimes identified by our results, revealing four regimes that have different feature sizes, phase curve amplitudes, and flow speeds. We discuss the limitations of our comparison with previous Hubble Space Telescope (*HST*) and Spitzer Space Telescope observations, some of which may have probed higher pressures than those we model here, and suggest that mid-infrared observations with the MIRI instrument James Webb Space Telescope (*JWST*) will be better suited for comparison to our simplified model. We conclude that the 2D model reveals a variety of large-scale circulation regimes that we hope will be useful for interpreting observations and for guiding more detailed modelling.

2 BROWN DWARF ATMOSPHERIC VARIABILITY

Brown dwarfs have masses from a few times the mass of Jupiter (M_J) up to roughly $80M_J$, with radii similar to the radius of Jupiter (R_J). They can be free-floating or orbit other bodies; in this study we will model isolated brown dwarfs and will not consider the effects of other bodies such as stars (Showman et al. 2020). Strongly irradiated brown dwarfs like those modelled in Lee et al. (2020) behave more like 'hot Jupiter' exoplanets. Brown dwarfs in binary systems may still behave like isolated brown dwarfs if their external forcing is weak compared to their internal temperature. Brown dwarfs are characterized into L, T, and Y types corresponding to their spectral features and temperature. These types span a range of temperatures from $<$600 to $>$2100 K. Despite their high masses, they are all more comparable to the giant planets of the Solar system than stars (Showman et al. 2020), so we use a model similar to those used previously for giant planets.

2.1 Observations of atmospheric variability

Atmospheric circulation may produce changes in an observable field like temperature or albedo, which can be observed with time-resolved measurements like thermal phase curves. Biller (2017) reviewed time-resolved observations of brown dwarfs, describing how surface inhomogeneities lead to variability in the observed light curves. Observing this variability is more feasible for more rapidly rotating objects because more rotations can be observed in a short time, sampling the spatial frequencies of the surface pattern more accurately. The thermal phase curve of a uniform brown dwarf with no surface features would be flat as it rotates. Stationary surface inhomogeneities due to temperature variations or clouds would produce a variable phase curve, with a constant period at the rotation period of the brown dwarf. Artigau et al. (2009) showed this for a T-dwarf, where the shape of its phase curve varied with time but its period was constant. This suggests that the inhomogeneities were stationary in position but varied in size with time.

Artigau (2018) showed how the magnitude of this observed variability can vary with wavelength, suggesting that the surface inhomogeneity corresponds to variations in several different atmospheric layers. This highlights how interpreting real observations will be more complex than the simple one-layer simulations in this study. For example, Yang et al. (2016) showed how light curves measured at different wavelengths can be out of phase with each other. This variation can present opportunities – Crossfield et al. (2014) used multiwavelength time-domain observations to derive a 2D map of the cloud distribution on Luhman 16B, and suggested that the dynamical time-scale of the atmosphere is approximately one Earth day.

Atmospheric circulation has been inferred from observations of time-resolved flux from planets in the Solar system. Simon et al. (2016) showed how banded zonal jets lead to multiple shifted periods in the periodograms of broad-band light curves of Neptune from the Kepler space telescope. They used a zonal velocity profile from Galperin & Read (2019) to estimate the latitude of the moving feature of each peak, as the shift depends on the angular velocity of the feature, which depends on both its velocity and latitude. Apai et al. (2017) fitted infrared Spitzer Space Telescope observations of several brown dwarfs with empirical models of varying surface flux, based on local spots or zonal bands. These shapes were inspired by similar morphologies on the giant planets of the Solar system like those in Simon et al. (2016). They compared the periodogram of the time-resolved thermal emission to the periodogram of light-curve observations of Neptune from Simon et al. (2016), suggesting that the brown dwarf's periodogram had a similar broad peak due to similar banded zonal jets.

Vos et al. (2020) measured variability like that in Apai et al. (2017) for several low-gravity L dwarfs with Spitzer phase curves, deriving periodograms and suggesting that variability was strongest for objects viewed equator-on. Zhou et al. (2022) observed a late L-type planetary-mass companion with extremely high variability. They combined observations with *HST* at different epochs to find a maximum flux variation of 33 per cent, with a variety of strong frequencies in the time-series flux. The variability could be reproduced by models based on zonally moving waves, stationary spots, or combinations of both.

Determining the exact velocities corresponding to different peaks in these observed periodograms requires knowledge of the rotation period of a brown dwarf. This is difficult to determine from a thermal phase curve as it may be affected by the motion of the part of the atmosphere being observed. It can be roughly inferred from the phase curve, such as in Apai, Nardiello & Bedin (2021) where the dominant peak in the periodogram was used to measure the rotation period of the brown dwarf Luhman 16B to be 5.28 hours. However, this peak may be moved away from the true period by atmospheric dynamics, and Apai et al. (2021) highlighted that the peak is broadened, which they suggest could be due to banded jet streams. Zhou et al. (2022) derived periodograms without a clearly dominant peak to ascribe to a rotational period, suggesting strong large-scale motion beyond variability due to stationary features on the rotating body.

Manjavacas et al. (2017) showed three peaks in the periodogram of the broad-band phase curve of the L-dwarf LP261-75B. They found a dominant period at 4.87 h which they suggest to be the rotation period of the brown dwarf. They also found two smaller peaks

at shorter periods, and suggested causes including heterogeneous cloud coverage. Allers et al. (2020) measured the first true rotation period of a brown dwarf from its radio emission. This was different to the rotational period measured from its infrared emission, by an amount corresponding to an eastward atmospheric motion of 600 ± 300 ms^{-1}. These measurements of absolute velocities, and the measurements of varying feature size and relative motion in other studies, motivate our modelling of the circulation regimes of brown dwarfs.

The photosphere at the wavelengths measured in a particular observation varies according to the spectral type of the brown dwarf, and can therefore lie within either or both of the convective and stably stratified layers. In particular, near-infrared wavelengths are expected to correspond partially or entirely to the convective layer. Morley et al. (2014a) modelled Y-dwarfs and found that the $1-6\,\mu$m photosphere is entirely within the convective zone. Burningham et al. (2017) found the near-infrared photosphere of two observed L-dwarfs to be at similarly deep pressures, between 1 and 10 bar. This is consistent with the modelling results of Phillips et al. (2020) for L and T dwarfs, who modelled a convective zone up to 3 bars that accounted for the majority of the near-infrared photosphere. Tremblin et al. (2015) suggested an even higher convective zone with a model of enhanced convection for Y and T dwarfs, which would put the entire near-infrared photosphere within the convective zone. *HST* observations with the WFC3 grism would almost certainly correspond to a photosphere in this deeper region (Yang et al. 2016).

All these different approaches find that the average near-infrared photosphere is partially or entirely below the stably stratified layer, so our direct link between this modelled layer and the observed phase curve is approximate for near-infrared wavelengths on average. Observations in specific bands can correspond better to the layer we simulate. For example, the *Spitzer* 3.6 and 4.5μm channels are near CH_4 and CO bands, respectively, as well as the water vapour continuum, so should probe pressures between 0.1 and 1 bar corresponding to the stratified layer (Morley et al. 2014b). The large-scale phase-curve variability in the *Spitzer* observations in these channels (Yang et al. 2016; Apai et al. 2017; Vos et al. 2020, 2022) implies thermal emission affected by an active weather layer supporting atmospheric dynamics, and would be difficult to explain with a purely convective layer. This issue will hopefully be addressed by time-series observations of brown dwarfs with the *JWST* MIRI instrument in the mid-infrared, which should probe lower pressures in more detail and correspond more directly to the expected stably stratified weather layer.

2.2 Models of atmospheric dynamics

Showman et al. (2020) reviewed the atmospheric dynamics of brown dwarfs and described their basic dynamical regimes as rotationally dominated with Rossby numbers $<<1$. Showman & Kaspi (2013) derived an analytical theory for the circulation of brown dwarfs, predicting global horizontal wind speeds of 10–300 ms^{-1}. Zhang & Showman (2014) modelled the dynamical variability of brown dwarfs using a shallow-water model with random small scale forcing, varying the forcing strength and radiative time-scale. They found two main regimes: one dominated by zonal jets and one dominated by small-scale vortices. They suggested that the small deformation radii of their simulations resulted in long-lived large-scale mid-latitude vortices rather than strong zonal jets.

Showman, Tan & Zhang (2019) used a 3D model with small-scale forcing, finding complex behaviour including a QBO-like circulation and zonal jets. Tan & Showman (2021b) showed that a cloud feedback mechanism can produce small-scale forcing with similar effects to those imposed by Zhang & Showman (2014). Tan & Showman (2021a) ran simulations of a global model with this cloud-based feedback mechanism. They varied the rotation period and the time-scale of dynamical drag, and found varying zonal jets and equatorial waves.

The atmospheric dynamics of simulated brown dwarfs have many similarities to those of giant gaseous planets. For idealized shallow-water models, the models and their outcomes are often identical or separated only by the choice of numerical parameters. Cho & Polvani (1996) showed the formation of banded jets and polar vortices in an unforced Jupiter-like shallow-water model that was initialized from turbulent flow. Showman (2007) used a similar model but forced it by injecting random storms like the model of Zhang & Showman (2014). They both showed the formation of similar banded jets and vortices, which can be present at different latitudes on the planet separated.

Brueshaber, Sayanagi & Dowling (2019) and Brueshaber & Sayanagi (2021) used a shallow-water model with similar random forcing to Zhang & Showman (2014) to investigate the formation of polar vortices on the giant planets of the Solar system. They modelled the polar region only, and varied parameters such as the Burger number and forcing strength to find regions of the parameter space that result in polar vortices. Their results were similar to those of Scott (2011), who showed that individual cyclones injected to a shallow-water model will migrate towards the pole if they have sufficient potential vorticity relative to the pole. This means that planets with stronger forcing and slower rotation rates will tend to accumulate cyclonic vorticity at their poles and form polar vortices.

Scott & Polvani (2007) used a spectral forcing formulation for a shallow-water model, injecting energy at small wavenumbers instead of injecting energy with individual storms. They showed the important effect of energy dissipation via either radiative relaxation, Rayleigh drag, or numerical hyperdiffusion on the zonal jets and the polar vortices. Scott & Polvani (2008) showed how a shallow-water system can develop equatorial superrotation (eastward equatorial flow) given appropriate radiative relaxation. This differed from the above studies, which generally formed westward equatorial flow.

All these previous modelling studies of brown dwarfs and giant planets identified zonal jets and vortices of varying size and position. We aim to describe how these features vary over the entire plausible parameter space of brown dwarf atmospheres in an idealized 2D model.

3 SHALLOW-WATER MODELLING

We use a one-layer, 2D shallow-water model to simulate brown dwarf atmospheres. As in Showman (2007) and Zhang & Showman (2014), this model represents the stably stratified weather layer, on top of a convective interior (Burrows, Sudarsky & Hubeny 2006). The shallow layer corresponds to the atmospheric mass higher that a given surface of constant potential density. This marks the boundary to the deep convective layer which we do not model apart from the forcing it applies to the stably stratified layer.

3.1 Dimensional model

The equations governing the shallow layer are (Vallis 2006):

$$\begin{aligned} \tfrac{D\mathbf{u}}{Dt} + \nabla\Phi + f\mathbf{k}\times\mathbf{u} &= 0, \\ \tfrac{D\Phi}{Dt} + \mathbf{u}\nabla\cdot\Phi &= \tfrac{\Phi_0-\Phi}{\tau_{\rm rad}} + S. \end{aligned} \tag{1}$$

In these equations $\frac{D}{Dt} \equiv (\frac{\partial}{\partial t} + \mathbf{u} \cdot \nabla)$ is the material derivative. The variables are the velocity $\mathbf{u}$, and the geopotential $\Phi = gh$, where g is the acceleration due to gravity and h is the height.

The model parameters are the equilibrium geopotential Φ_0, the radiative time-scale $\tau_{\rm rad}$, and the Coriolis parameter $f = 2\Omega\cos\theta$, where the rotation rate is Ω and the latitude is θ. The radius a is also a parameter via the spatial derivatives.

We solve these equations using the spectral dynamical core of the GFDL Flexible Modelling System FMS[1] (Gordon & Stern 1982). We use a resolution of T170 (with 512 longitude points and 256 latitude points). This is equivalent to approximately 0.7° at the equator, as used in Zhang & Showman (2014). The model applies a fourth-order hyperdiffusion to the vorticity field with a strength set by a coefficient ν.

We follow Showman (2007), Zhang & Showman (2014), and Brueshaber et al. (2019) and force the model with randomly located 'storms' corresponding to convective events. These storms add up to produce a net tendency S in the geopotential field:

$$S = \sum_i \frac{\partial(\Phi)}{\partial t}\Big|_{\rm i} = \sum_i S_0 \exp\left[-\frac{|\mathbf{r} - \mathbf{r_i}|^2}{r_s^2} - \frac{(t - t_i)^2}{\tau_s^2}\right], \tag{2}$$

where i denotes each storm in a series of randomly generated storms with time-scales $\tau_{\rm s}$, with constant intervals $\tau_{\rm int}$ separating their times t_i, which appear randomly over the surface of the sphere with positions r_i. We remove the overall tendency this adds to the mean geopotential by applying a uniform forcing everywhere, opposite to the total area-integrated tendency introduced by each storm (Brueshaber et al. 2019):

$$\frac{\partial(\Phi)}{\partial t}\Big|_{\rm global} = -\frac{1}{4\pi a^2}\int \sum_i \frac{\partial(\Phi)}{\partial t}\Big|_{\rm i} {\rm d}A. \tag{3}$$

This keeps the global mean value of Φ fixed at Φ_0, which keeps the Rossby deformation radius constant and avoids model instability caused by the mean geopotential becoming too small or large. The total model forcing S is then:

$$S = \frac{\partial(\Phi)}{\partial t}\Big|_{\rm global} + \sum_i \frac{\partial(\Phi)}{\partial t}\Big|_{\rm i}. \tag{4}$$

The model is damped by relaxation towards the equilibrium geopotential Φ_0, representing the radiative cooling of the atmosphere. We do not include the 'R' term used in Zhang & Showman (2014), which represents the effect of transport between the modelled layer and the deep layer on the zonal momentum. We choose to omit this term as it is an additional physical forcing with unknown effects, and we aim to understand the effects of the random forcing fully before introducing further forcing terms. Further work could include this term as an additional forcing, and investigate its possible effect on the zonal flow.

We set the forcing strength to be $S_0 = 0.1\Phi_0/\tau_{\rm s}$ so that the height tendency is a constant fraction of the equilibrium geopotential. This makes the forcing term non-dimensional as required, but means we have to choose a specific value for the relevant fraction. Given the idealized nature of our modelling, we choose an order of magnitude value. Using a forcing of $0.1\Phi_0/\tau_{\rm s}$ produces appropriate perturbations that are on the order of the equilibrium geopotential height. Using a larger value of $1.0\Phi_0/\tau_{\rm s}$ caused some of the simulations to become unstable, as the perturbations can become larger than the thickness of the modelled layer.

[1] gfdl.noaa.gov/fms

Using a smaller value (not shown) produced circulation regimes that were identical or qualitatively similar to the regimes we identify in Section 6, apart from their absolute magnitude, indicating that the responses vary approximately linearly with forcing. In Section 6, we focus mainly on the non-dimensional morphology of the circulation regimes, so the absolute magnitude of the perturbations is not crucial to our conclusions. In reality, the variations in atmospheric height in our model, corresponding to variations in temperature in a 3D model, could lead to significantly larger variations in flux due to the presence or absence of clouds. We therefore suggest that while it would be useful to explore the effect of the fractional forcing strength in future work, it has a weaker effect on the circulation regimes than the key parameters like rotation rate, radius, and so on, which we investigate here via the non-dimensional parameters.

We set the length-scale of the storms r_s to be 2° of longitude at the equator, the same as the lower resolution simulations in Showman (2007). If we assume that the diameter of each storm is twice this length-scale, each storm is resolved by about six grid points. The length-scale of the storms r_s and their strength S_0 are model parameters that we set constant, which are not included in our later non-dimensionalization. We suggest that these are reasonable assumptions, as we only need the storms to be much smaller than any features of observable scale. For the forcing strength, we need its order of magnitude to be large enough to produce features of observable strength, and also to be small enough to not produce unphysical features larger than the equilibrium height.

The model then has five variable parameters left – equilibrium geopotential Φ_0, rotation rate Ω, radius a, radiative time-scale $\tau_{\rm rad}$, and hyperdiffusion strength ν. This leaves a 5D parameter space to explore in our aim to determine how the circulation regimes of brown dwarfs depend on their properties. In the next section, we describe how we reduce this to two parameters by non-dimensionalizing the model.

3.2 Non-dimensional model

We can non-dimensionalize equations (5) by substituting in the following non-dimensional variables:

$$\begin{aligned} \hat{\Phi} = \Phi/\Phi_0 &= \tfrac{\Phi}{2\Omega u_0 a}, \\ (\hat{u}, \hat{v}) &= (\tfrac{\hat{u}}{u_0}, \tfrac{\hat{v}}{u_0}), \\ \hat{t} &= 2\Omega t, \\ \hat{f} &= \tfrac{f}{2\Omega}. \end{aligned} \tag{5}$$

Circumflexes denote non-dimensional parameters. All of the time-scales τ are non-dimensionalized in the same way as the time t. The scale of the geopotential $\Phi_0 = 2\Omega u_0 a$ is derived by assuming thermal wind balance (Mitchell & Vallis 2010). If we also non-dimensionalize the spatial derivatives with a, this leads to the following non-dimensional equations:

$$\begin{aligned} \tfrac{\partial \hat{\mathbf{u}}}{\partial \hat{t}} + {\rm Ro_T}\,\hat{\mathbf{u}} \cdot \nabla\hat{\mathbf{u}} + \nabla(\hat{\Phi}) + \hat{f}\mathbf{k} \times \hat{\mathbf{u}} = 0 \\ \tfrac{\partial(\hat{\Phi})}{\partial \hat{t}} + {\rm Ro_T}\,\hat{\mathbf{u}} \cdot \nabla\hat{\Phi} = \tfrac{1-\hat{\Phi}}{\hat{\tau}_{\rm rad}} + \hat{S} \end{aligned} \tag{6}$$

where $\hat{S} = S/\Phi_0 = S/(\hat{\tau}_{\rm rad}^2 {\rm Ro_T})$. These equations then only depend on the parameters:

$$\begin{aligned} &\text{Thermal Rossby Number} : {\rm Ro_T} = \tfrac{u_0}{2\Omega a} = \tfrac{\Phi_0}{(2\Omega a)^2} \\ &\text{Non-dimensional Radiative Time-scale} : \hat{\tau} = 2\Omega\tau \\ &\text{Ekman Number} : E_k = \tfrac{\nu}{2\Omega} \end{aligned} \tag{7}$$

The thermal Rossby number measures the ratio of the inertial force (due to the thermal wind) to the Coriolis force (due to

rotation). The non-dimensional radiative time-scale compares the radiative time-scale to the rotation rate of the atmosphere. The Ekman number measures the strength of the hyperdiffusion, and we set it to be constant so that the hyperdiffusion stabilizes the model but does not affect the large-scale circulation. Given constant E_k, the non-dimensional model then only depends on $\mathrm{Ro_T}$ and $\hat{\tau}$. The exact magnitude of the variables Φ, u, and v depend on the separate dimensional parameters such as a, but the morphology (the circulation regime) will be identical given identical $\mathrm{Ro_T}$ and $\hat{\tau}$. This means that the ($\mathrm{Ro_T}$, $\hat{\tau}$) parameter space contains the entire range of behaviour possible in this model. We verified that simulations with different dimensional parameters like a and Ω, but the same $\mathrm{Ro_T}$ and $\hat{\tau}$, give identical results once all output variables are non-dimensionalized.

3.3 Dimensional parameter space

Our non-dimensional ($\mathrm{Ro_T}$, $\hat{\tau}$) parameter space is determined by the dimensional ranges of the rotation rate Ω, radiative time-scale τ, and equilibrium geopotential Φ_0. In all the following estimates we err on the side of a larger parameter space, to ensure that we capture all the behaviour possible in our model. We assume that the rotation rates are in the range 10^{-5} s^{-1} $< \Omega <$ 10^{-3} s^{-1} (Reiners & Basri 2008). We assume that the radius a is of the order of 10^8 m. We can then estimate the plausible ranges of the radiative time-scale τ_{rad} and equilibrium geopotential Φ_0 from Ω and a. For τ_{rad}, following Zhang & Showman (2014), we estimate that:

$$\tau_{\mathrm{rad}} \sim \frac{p}{g}\frac{c_p}{4\sigma T^3}. \tag{8}$$

We assume that the brown dwarfs have a radiating level 10^4 Pa (Showman 2007), gravity g from 500 to 3000 ms^{-2} (Burrows et al. 2006), heat capacity $c_p = 14\,300$ J kg^{-1} K^{-1}, and temperatures varying from 100 to 2200 K (Zhang & Showman 2014). This gives an upper bound on the radiative time-scale of 10^9 s, and a lower bound of 10^2 s. However, we found that extremely short radiative time-scales gave identical results as they were much shorter than any other time-scale in the model (generally set by the range of rotation rates). So we assume that our actual lower bound is 10^6 s, giving a final range of dimensional radiative time-scales 10^6 s $< \tau_{\mathrm{rad}} < 10^9$ s.

Next, we estimate the range of equilibrium geopotentials by setting Φ_0 such that it results in a Rossby deformation radius $L_R = \sqrt{\Phi_0}/f$, equal to the deformation radius $L_R = NH_p/f$ expected from the vertical structure of a typical brown dwarf atmosphere (Zhang & Showman 2014). In this expression, $H_p = R_g T/\mu g$ is the pressure scale height and the Brunt–Väisälä frequency is:

$$N = \left[\frac{g}{T}\left(g/c_p + \mathrm{d}T/\mathrm{d}z\right)\right]^{1/2} = g\left[\gamma/\left(c_p T\right)\right]^{1/2}, \tag{9}$$

where $\gamma = [1 + (c_p/g)\mathrm{d}T/\mathrm{d}z]$ is determined by the vertical temperature structure of the atmosphere. Zhang & Showman (2014) estimate $\gamma \sim 1$ for a typical brown dwarf. Equating these two expressions for L_R gives:

$$\Phi_0 = (fL_R)^2 = \gamma\kappa^2 c_p T, \tag{10}$$

where $\kappa = R/\mu c_p \sim 2/7$. With a temperature range 100 K $< T <$ 2200 K, this gives a range of equilibrium geopotentials 10^5 m^2 s^{-2} $< \Phi_0 <$ 10^7 m^2 s^{-2}. We follow Zhang & Showman (2014) in expanding the upper bound of this to 10^8 to reflect the potential range of vertical wavelengths, giving a final range of 10^5 m^2 s^{-2} $< \Phi_0 <$ 10^8 m^2 s^{-2}.

3.4 Non-dimensional parameter space

Using the plausible ranges of dimensional parameters, we can estimate the range of $\mathrm{Ro_T}$ and $\hat{\tau}$ that represents all plausible brown dwarf circulation patterns in our model.

The non-dimensional radiative time-scale is $\hat{\tau} = 2\Omega\tau$, so the range of rotation rates 10^{-5} s^{-1} $< \Omega <$ 10^{-3} s^{-1} and the range of radiative time-scales 10^6 s $< \tau <$ 10^9 s give a range of non-dimensional radiative time-scales $10^1 < \hat{\tau} < 10^6$. The thermal Rossby number is $\mathrm{Ro_T} = \Phi_0/(2\Omega a)^2$, so the range of rotation rates 10^{-5} s^{-1} $< \Omega <$ 10^{-3} s^{-1}, the range of geopotentials 10^5 m^2 s^{-2} $< \Phi_0 <$ 10^8 m^2 s^{-2}, and a radius of the order of 10^8 m give a range of thermal Rossby numbers $10^{-5} < \mathrm{Ro_T} < 10^2$.

To run a simulation with a particular combination of $\mathrm{Ro_T}$ and $\hat{\tau}_{\mathrm{rad}}$, we arbitrarily choose $\Omega = 10^{-4}$ and $a = 10^7$. The non-dimensional model output is independent of these choices. We choose the Ekman number to be constant at $E_k = 10$, which gives a weak enough hyperdiffusion that our choice does affect the large-scale circulation, so we do not need to vary this non-dimensional parameter.

As the non-dimensional radiative damping time-scale $\hat{\tau}_{\mathrm{rad}}$ is our parameter of interest, we set $\hat{\tau}_{\mathrm{s}} = \hat{\tau}_{\mathrm{int}} = 20$. This is because our only requirement is that these time-scales are small compared to the other time-scales (for example, our smallest non-dimensional radiative time-scale is $\hat{\tau}_{\mathrm{rad}} = 100$), producing constant small-scale forcing.

For a brown dwarf with $\Omega = 10^{-4}$, this corresponds to a dimensional time-scale of 10^5 s, which is consistent with the estimated range of convective time-scales used in Zhang & Showman (2014) for a similar shallow-water model of a brown dwarf. In addition, it is consistent with the roughly 10 h time-scale of the 1D radiative feedback variability in Tan & Showman (2019). It is also the same as the value used in Showman (2007) for a similar shallow-water model of Jupiter and Saturn, which was motivated by observations. It could be useful to investigate the effect of varying this time-scale in future work, but we suggest that the effect will be weaker than the parameters like rotation rate and radius, as long as the storm time-scale is shorter than the other time-scales of the modelled system.

We then calculate $\Phi_0 = \mathrm{Ro_T}(2\Omega a)^2$ and $\nu = 2\Omega E_k$ and run each test in our non-dimensional parameter ranges $10^1 < \hat{\tau} < 10^6$ and $10^{-5} <$ $\mathrm{Ro_T} < 10^2$, with a test at each order of magnitude on each axis. The model runs with these dimensional parameters as inputs, and then we divide all the output variables by their scales listed in Section 3.2 to retrieve the non-dimensional output. We spin up the model for 10 000 Earth days, which in our non-dimensional parameter space is more than twice as long the radiative time-scales of all the tests, except the tests with $\hat{\tau}_{\mathrm{rad}} = 10^6$. After this, we output data for 10 model days every 2 model hours (non-dimensionally, 13.75 rotations outputting data every 0.115 rotations). The length of this data period is chosen to include at least as many rotational periods as any current observations, and the cadence is chosen to capture any of the large-scale motions present in the atmospheres.

4 CIRCULATION RESULTS

In this section, we describe the results of the suite of simulations in our non-dimensional parameter space. We show the instantaneous height, potential vorticity, and zonal-mean zonal velocity as a function of the non-dimensional parameter space.

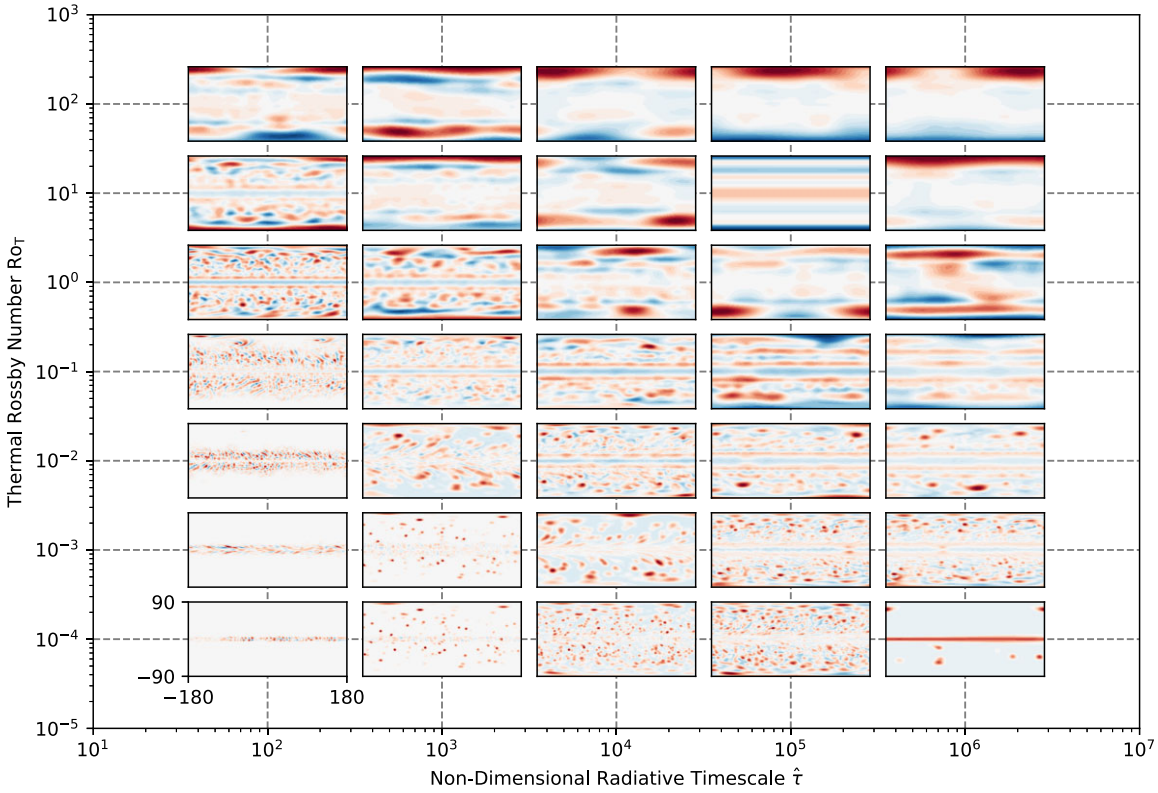

Figure 1. The instantaneous non-dimensional height field after 10 000 d in the parameter space of thermal Rossby number Ro_T versus non-dimensional radiative time-scale $\hat{\tau}_{rad}$. The colour scale of each plot is normalized to the maximum deviation from the mean height of each simulation.

4.1 Height

Fig. 1 shows the instantaneous height field of each simulation. They are all forced identically with small-scale storms but end up with very different height fields due to their different circulation regimes, determined by the two non-dimensional parameters that define each test.

We can divide the height fields in Fig. 1 into four regimes. Tests with a low Ro_T and a low $\hat{\tau}_{rad}$ are relaxed very quickly back to a state of uniform Φ, so have height fields either dominated by the recent short-term small-scale forcing, or even height fields close to uniformity. Section 6 will show that this is an extreme regime unlikely to correspond to real brown dwarfs, but if these were real their observational features would be dominated by the local radiative properties of the atmosphere and large-scale atmospheric dynamics would not be important.

Tests with a high Ro_T and a low $\hat{\tau}_{rad}$ are also relaxed quickly towards equilibrium, but still form strong large-scale atmospheric dynamics. Energy is still injected at the small scale of the storms, and then an inverse cascade transfers this energy to larger scales, truncating at a relatively large scale due to the larger Rhines scale in this regime (corresponding to low rotation rate, or high equilibrium geopotential; Wang et al. 2018). These tests are not zonally uniform as the radiative relaxation is still relatively fast compared to rotational processes.

Tests with a low Ro_T and a high $\hat{\tau}_{rad}$ have little effect from atmospheric dynamics, but have a relatively long radiative relaxation time. They are dominated by the built-up random forcing as well as medium-scale dynamical features such as equatorial jets and mid-latitude waves. There is a mixture of zonally uniform features like jets and non-uniform features like waves. For comparison, Jupiter has roughly $Ro_T = 10^{-2}$ and $\hat{\tau}_{rad} = 10^5$ (Showman 2007). In the simulation in Fig. 1 with these non-dimensional parameters there is a mixture of large-scale waves and zonal bands corresponding to jets, roughly matching the real large-scale morphology of Jupiter.

Tests with a high Ro_T and a high $\hat{\tau}_{rad}$ transfer energy very effectively to large scales, and have a relatively long radiative relaxation time-scale so form very large, somewhat zonally uniform features. This regime would result in brown dwarfs with strong zonal flow.

4.2 Zonal-mean zonal velocity

Fig. 2 shows the instantaneous zonal-mean zonal velocity for our parameter space. We have dimensionalized the model results to show what the speed would be for a typical brown dwarf with a radius of 7×10^7 m and a rotation rate of 10^{-4} s^{-1}.

In general, the tests with high $\hat{\tau}_{rad}$ have strong jets and vice versa. This is easily explained as the vortices introduced by the random forcing are damped more strongly if $\hat{\tau}_{rad}$ is low, so are suppressed before they can form zonal jets via an inverse cascade of kinetic energy to larger scales (Rhines 1975). In this effect, sufficiently large β (the local meridional gradient of the Coriolis parameter f) leads to an inverse transfer of energy from small scales to large-scale features that are elongated zonally with a meridional width scale $(U/\beta)^{1/2}$.

Tests with high Ro_T have strong jets as the Rhines scale, at which the inverse energy cascade terminates, approaches the planetary scale. This is consistent with the results of Showman (2007), where zonal jets do not form in shallow-water simulations with small equilibrium geopotentials. Zhang & Showman (2014) also identified this effect shallow-water simulations of brown dwarf atmospheres,

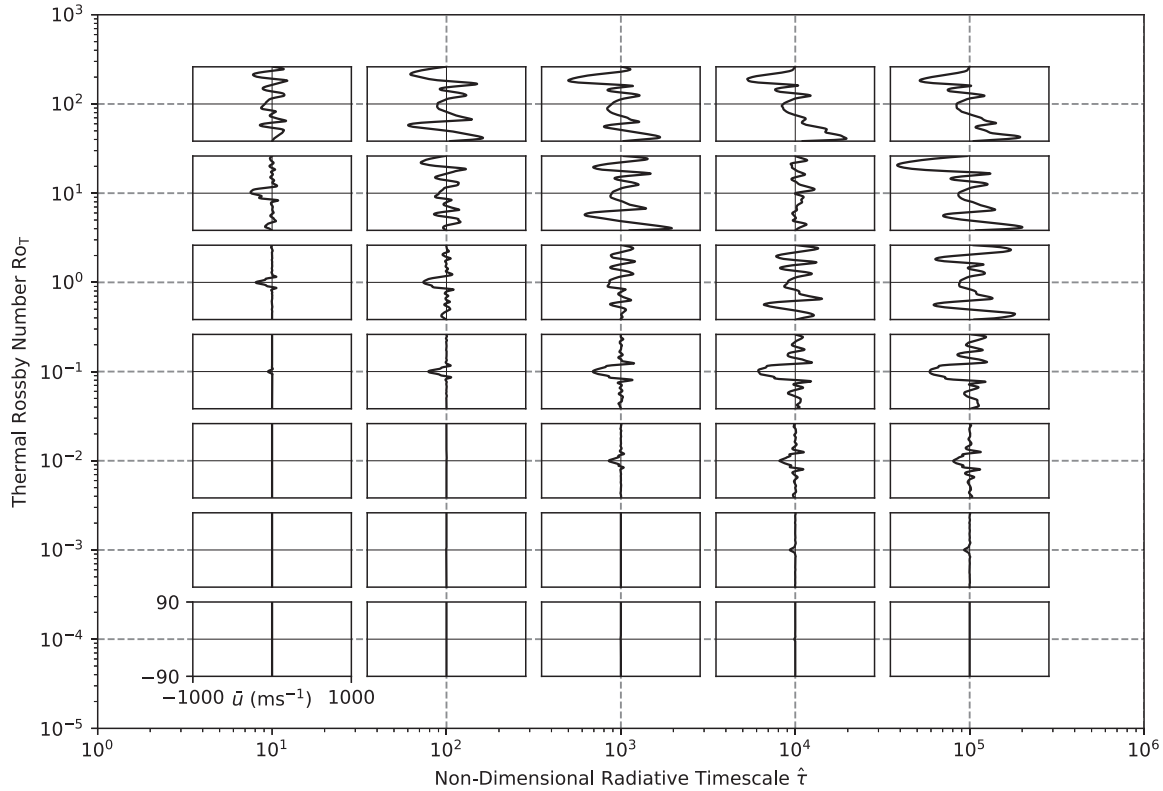

Figure 2. The instantaneous dimensional zonal-mean zonal velocity after 10 000 days in the parameter space of thermal Rossby number Ro_T versus non-dimensional radiative time-scale $\hat{\tau}_{rad}$. To give physical context for the non-dimensional velocities, we have dimensionalised the velocity to show what the speed would be for a brown dwarf with a radius of 7×10^7m, and a rotation rate of 10^{-4}s^{-1}. The x-axis of each subplot is limited to a dimensional velocity of 1000ms^{-1} in each direction.

showing a regime transition between jet-dominated and vortex-dominated atmospheres. Showman (2007) points out that due to the effect of latitude on the Rhines scale, there may be a latitude below which the Rhines effect forms zonal jets, and above which it is suppressed and vortices dominate. This may explain why our tests with intermediate Ro_T have zonal jets at the equator only.

4.3 Potential vorticity

Tan & Showman (2021a) found polar vortices in their 3D simulations of brown dwarfs. Brueshaber et al. (2019) used a shallow-water model to investigate the polar vortices of the giant planets of the Solar system, which vary from single cyclones (Neptune, Uranus and Saturn) to regularly spaced multiple vortices (Jupiter). The similarities between the atmospheres of giant planets and brown dwarfs suggests that polar vortices could be an important feature of the atmospheres of brown dwarfs. We look for polar vortices in the non-dimensional eddy potential vorticity (PV) $\hat{Q}_e$ fields, defining this quantity as the deviation from the mean PV, in the same way as the results of the shallow-water models of Brueshaber et al. (2019):

$$Q_e = Q - \langle Q \rangle, \tag{11}$$

where the PV is

$$Q = \frac{\zeta + f}{h}, \tag{12}$$

where ζ is the relative vorticity, f is the Coriolis parameter, and h is the height. The mean PV is

$$\langle Q \rangle = \frac{f}{\langle h \rangle}. \tag{13}$$

We then normalize the eddy PV like Brueshaber et al. (2019) to define the non-dimensional quantity:

$$\hat{Q}_e = (Q - \langle Q \rangle)\frac{\langle h \rangle}{2\Omega} = \left[\frac{\zeta + f}{h} - \frac{f}{\langle h \rangle}\right] \cdot \frac{\langle h \rangle}{2\Omega}, \tag{14}$$

which is plotted in Fig. 3, showing the instantaneous $\hat{Q}_e^*$ of each simulation, calculated with the *windspharm* code package (Dawson 2016). Tests with a low Ro_T or a low $\hat{\tau}_{rad}$ either do not transfer energy to large scales efficiently, or are relaxed towards equilibrium too fast for polar vortices to form.

Tests with a high Ro_T and a high $\hat{\tau}_{rad}$ can support long-term vortices that migrate towards the pole, forming a large polar vortex. The polar vortices in Fig. 1 are not exactly centred on the pole, migrating around to some extent. Their close alignment with the rotation axis of the brown dwarf means that they do not strongly affect the phase curve. The suggestion of Apai et al. (2021) that polar vortices could explain phase curve variability is unlikely if the vortices are located near the pole like in our results, although polar vortices could still play an important role in the atmosphere of the brown dwarf as a whole.

The formation and maintenance of polar vortices such as those on Jupiter and Saturn is complex in both reality and models (Brueshaber et al. 2019; Cai, Chan & Mayr 2021; Mitchell et al. 2021) and our model cannot reproduce them exactly. The idealized model of Showman (2007) did not reproduce the geometric pattern of vortices

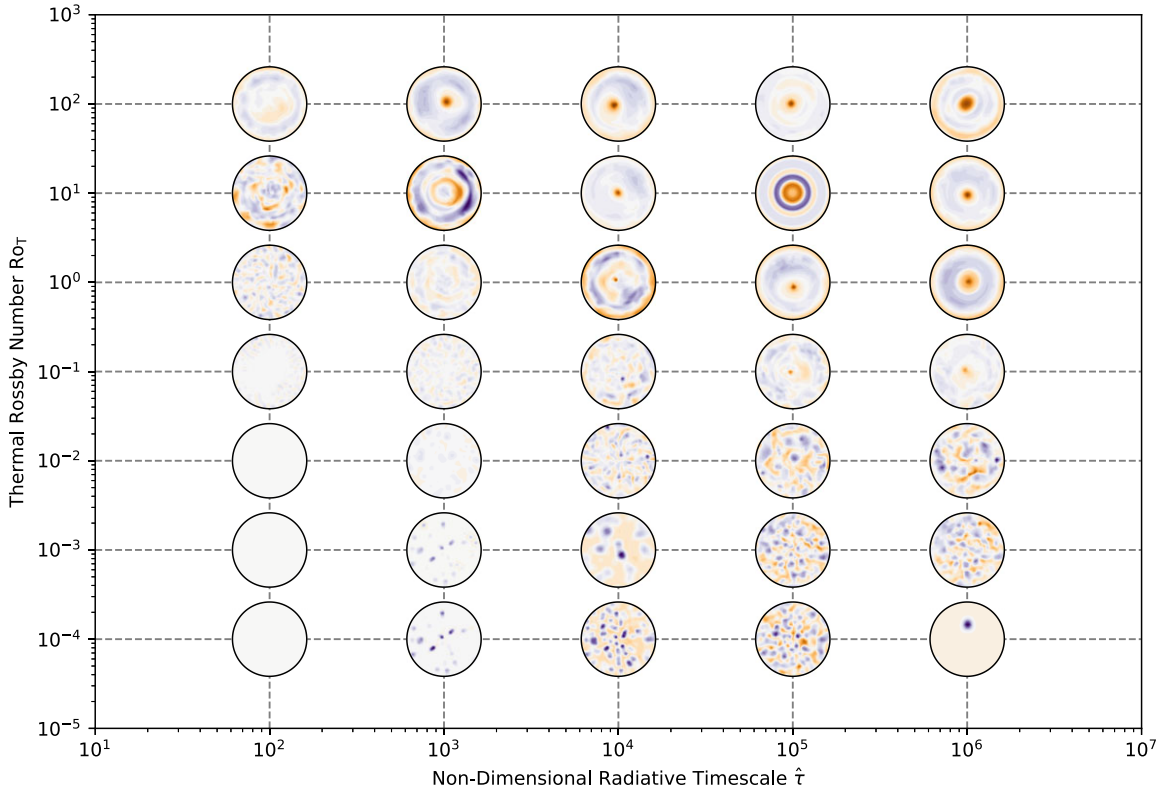

Figure 3. The instantaneous non-dimensional eddy potential vorticity field after 10 000 days in the parameter space of thermal Rossby number $\mathrm{Ro_T}$ versus non-dimensional radiative time-scale $\hat{\tau}_{\mathrm{rad}}$. Each plot is centred on the north pole of the brown dwarf and the outer edge is 45°N. The colour scale of each plot is normalized to the maximum absolute magnitude of the eddy potential vorticity of each simulation.

on Jupiter, so it is possible that brown dwarfs support polar vortices that are too complex to be reproduced by our 2D model.

5 SIMULATED OBSERVATIONAL RESULTS

In this section, we plot simulated observations of our suite of tests, showing their phase curves and the resulting periodograms. Studies such as Allers et al. (2020) and Apai et al. (2017) have used observations like these to estimate rotation periods, sizes of surface features, and wind speeds.

5.1 Phase Curves

Our idealized model has no explicit radiative transfer, so we follow Zhang & Showman (2014) and emulate the thermal phase curve by inserting the height field in place of the outgoing flux. This assumes that variations in height correspond to variations in temperature and so determine the location and size of variations in outgoing thermal flux. Our main concern is the size, position, and velocity of the variations in height in the atmosphere, rather than their absolute magnitude, so this approximation suits our purposes.

Our simplified approach assumes that the simulated thermal phase curve corresponds entirely to emission from the stably stratified layer represented by our shallow-water model. However, as discussed above, thermal emission (particularly at near-infrared wavelengths) is often thought to probe a photosphere partially or entirely in the convective zone, below the weather layer (Morley et al. 2014a; Burningham et al. 2017; Phillips et al. 2020). Specific bands can probe lower pressures, such as the Spitzer 3.6μm and 4.5μm channels (Morley et al. 2014b; Yang et al. 2016), but may also be affected by deeper convective layers. These phase curves should therefore be thought of as a simplified model of the maximum observable variability for a given circulation regime. The observations with Spitzer described above would only partially (or not at all) probe the simulated layer, so would show weaker variability. However, the feature size and wind speeds implied by the variability would be the same even if it only partially contributed to the total emission. Observations in the mid-infrared with the MIRI instrument on *JWST* will hopefully resolve this issue by measuring the thermal emission from lower pressures (Tang et al. 2021).

With this caveat in mind, we use the height field in the following expression for time-resolved flux $\bar{F}(t)$ (Adams, Millholland & Laughlin 2019):

$$\bar{F}(t) = \iint g h(t) V(\theta, \phi) \mathrm{d}\theta \mathrm{d}\phi, \tag{15}$$

where $V(\theta, \phi)$ is the normal vector $\hat{n}$ to each cell at longitude and latitude (θ, ϕ), resolved along the line of sight of the observer $\hat{r}_{\mathrm{obs}}$:

$$V = \begin{cases} \hat{n} \cdot \hat{r}_{\mathrm{obs}}, & \hat{n} \cdot \hat{r}_{\mathrm{obs}} \geq 0 \\ 0, & \hat{n} \cdot \hat{r}_{\mathrm{obs}} < 0, \end{cases} \tag{16}$$

where the point $(\phi_{\mathrm{obs}}, \theta_{\mathrm{obs}})$ facing the observer is:

$$\begin{aligned} \phi_{\mathrm{obs}} &= -\Omega t \\ \theta_{\mathrm{obs}} &= \epsilon, \end{aligned} \tag{17}$$

where ϵ is the viewing angle (0 is equator-on and $\pi/2$ is pole-on). Fig. 4 shows the phase curves with $\epsilon = 0$ over four rotations for each of our simulations. We normalize each phase curve to fill the y-axis of its plot as we are not primarily concerned with their absolute

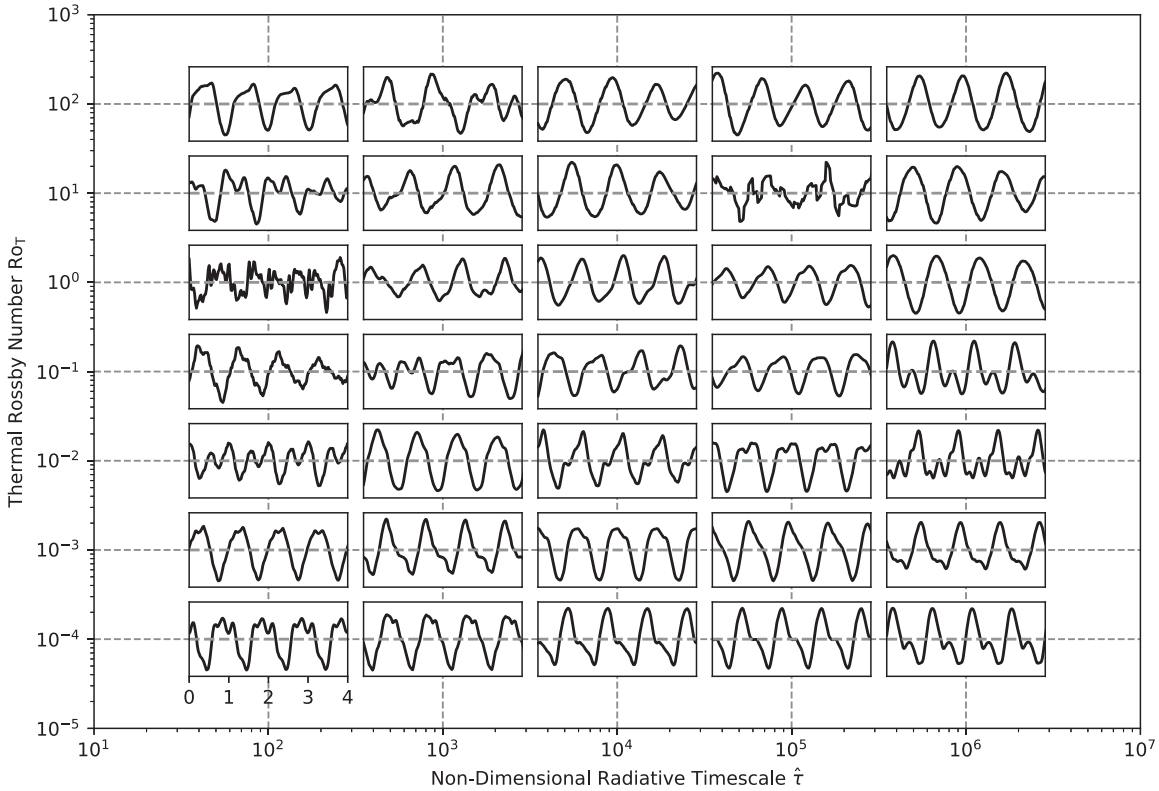

Figure 4. The phase curves in the parameter space of Ro_T versus non-dimensional radiative time-scale $\hat{\tau}_{rad}$, calculated by using the height field in place of an outgoing flux. The y-axis of each phase curve is scaled to fit its amplitude, as we are interested in the shapes and periods present instead of the absolute amplitude. The actual amplitudes of each phase curve are shown later in Fig. 6.

magnitude. We later show the actual amplitude of each phase curve in Fig. 6 as a fraction of the total emission.

Most of the phase curves have consistent form over the four orbits shown here. This supports studies like Apai et al. (2017) that use observations over a few days, or several rotations, of a brown dwarf. Some of the phase curves vary from orbit to orbit; these are correlated with the simulations with high Ro_T which have strong banded zonal flows that traverse the circumference of the brown dwarfs on time-scales comparable to their rotation. This means that features move significant distances at different speeds or directions so the height field changes notably from one rotation to the next.

Conversely, the simulations with low Ro_T have almost no mean velocity so their features are largely stationary from one orbit to the next. These simulations are still not purely sinusoidal, with regular modulation to the sinusoidal variation every rotation. This is due to spatially higher order features in the height fields shown in Fig. 1, which will become clearer in the next section. Despite the averaging inherent in the phase curve, there is a lot of dynamical variation in their shapes, particularly in the upper left corner of Fig. 4 where some of the simulated phase curves appear close to random noise. In the next section we will show how calculating periodograms for each simulation links their atmospheric dynamics to the form of their phase curve.

5.2 Periodograms

This section shows the Lomb–Scargle periodograms corresponding to the phase curves in Section 5.1 (Lomb 1976; Scargle 1982). We could have used a Fourier power spectrum instead of a Lomb–Scargle periodogram because we have uniformly sampled data, but chose to use the latter as it is the method used in observational analyses (Apai et al. 2017; Allers et al. 2020).

The periodograms show the frequencies present in each phase curve. More specifically, they show the frequencies present in the convolution in phase of the moving field viewed by the observer with the time-dependent height field. This means that they are a multiplication of the frequency of the rotation of the brown dwarf with the spatial frequency of the surface height field and the frequencies of the motion of its surface. This leads to several ways in which the periodogram deviates from a single peak at the rotation period of the brown dwarf.

The first source of additional peaks is higher order spatial frequencies. A brown dwarf with a static sinusoidal variation in height with wavenumber 1 in longitude will produce a single peak in its periodogram at its rotation period. If the variation in height is sinusoidal with wavenumber 2, the periodogram will have a single peak at half its rotation period, potentially misrepresenting its true rotation rate. Apai et al. (2017) measures periodograms with notable additional peaks at half the dominant periods. In the same way, if features composed of multiple wavenumbers are present, multiple peaks will be present in the periodogram.

The second source of additional peaks is atmospheric motion. If there is a single stationary spot in an otherwise uniform field, there will be a dominant peak at the rotation period of the brown dwarf. If a single spot is moving east or west (with or against the rotation direction), the period of its modulation of the emission will be shifted

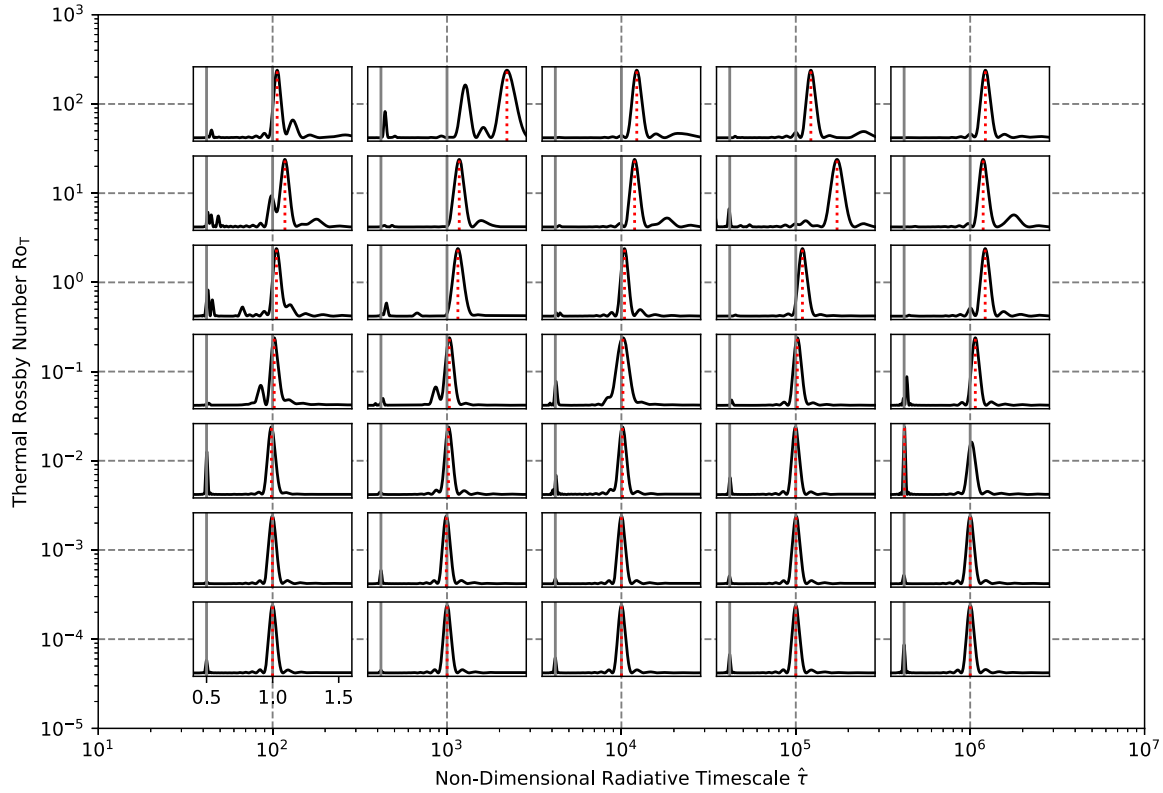

Figure 5. The Lomb–Scargle periodograms for the phase curves in Fig. 4 in the parameter space of Ro_T versus non-dimensional radiative time-scale $\hat{\tau}_{rad}$. The periodograms are calculated using the full 13.75 rotations of the brown dwarfs (more than are plotted in Fig. 4). Vertical lines show the rotation period and half-period of each simulation.

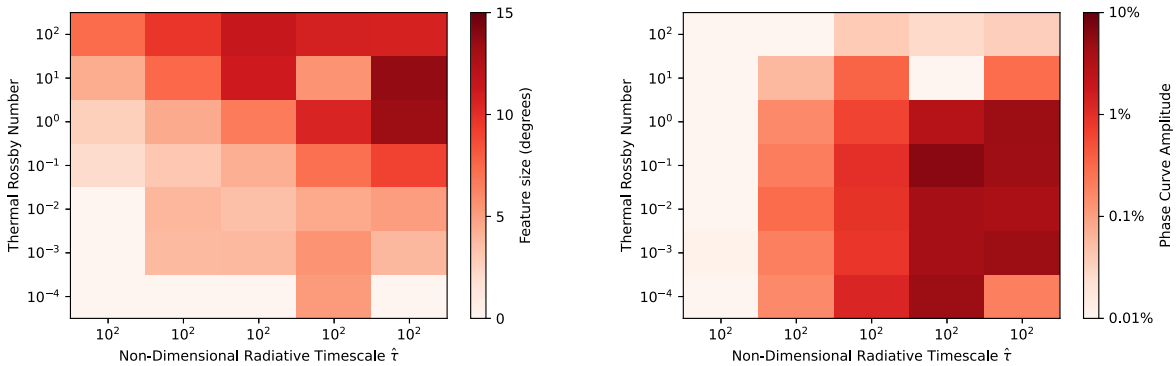

Figure 6. The size of the dominant energy-containing length-scale (left) and the fractional phase curve amplitude (right) in each simulation. The amplitude is the maximum minus the minimum of the phase curve, divided by its mean and expressed as a percentage. We set the dominant length-scale to be zero for simulations with maximum dimensional geopotential perturbations of less than 1000 $m^2\ s^{-2}$ (assuming a radius of 7×10^7 m and a rotation rate of $10^{-4}\ s^{-1}$), as otherwise the analysis picks up negligible features. This cutoff means that we do not measure features in some of the plots in the bottom left corner of Fig. 1.

to shorter or longer periods respectively, according to:

$$P' = \left(\frac{1}{P} + \frac{v}{2\pi r \cos\phi_0} \right)^{-1} \tag{18}$$

where P' is the period of the moving feature, P is the rotation period of the brown dwarf, v is the zonal velocity of the feature (where positive is eastward), r is the radius, and ϕ_0 is the latitude of the moving feature. Moving second-order spatial features (with periodogram peaks at half the rotation period of the brown dwarf) will be shifted in the same way, leading to degeneracies in explaining the source of shifted or additional peaks in the periodogram.

Fig. 5 shows the Lomb–Scargle periodograms for the phase curves in Fig. 4, calculated using 13.75 rotations of the brown dwarfs. The maximum of each periodogram is normalized to 1. The periodograms with low Ro_T are dominated by a single peak at the rotation period of the brown dwarf. Fig. 2 shows that these simulations have almost no zonal-mean zonal velocity, and we found no other features with significant motion. The peaks also have small amplitudes (not shown relative to the other plots) due to their small perturbations in their height field.

The simulations with intermediate Ro_T have larger half-period peaks corresponding to wavenumber-2 spatial features. They also

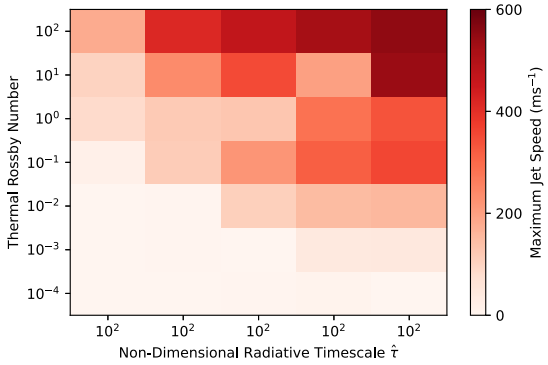

Figure 7. The maximum zonal-mean zonal wind speed in each simulation. The simulations with large $\mathrm{Ro_T}$ and $\hat{\tau}_{\mathrm{rad}}$ have faster maximum jets speeds. The direction of these varies as shown in Fig. 7, with westward equatorial jets for intermediate $\mathrm{Ro_T}$ and variable banded jets for high $\mathrm{Ro_T}$.

have wider central peaks corresponding to zonal flows. The simulations with large $\mathrm{Ro_T}$ have even wider peaks due to their banded jets, and even have some separate peaks or main peaks totally shifted away from their rotation period. For example, the simulation with $\mathrm{Ro_T} = 10^{1}$ and $\hat{\tau}_{\mathrm{rad}} = 10^{-3}$ has its strongest peak at about a 10 per cent longer period than its rotational period, which corresponds to westward atmospheric motion of about 600ms^{-1} at the equator (or slower motion nearer the pole) according to equation (18). It is more likely that shifts due to atmospheric motion correspond to motion near the equator, given the weighting of the phase curve with latitude—fast motion at the pole would produce a signal with very small magnitude compared to equatorial features.

Overall, brown dwarfs with higher rotation rates, higher surface gravity, small radii, and lower temperatures, are more likely to have shifted or additional peaks in their periodograms due to stronger atmospheric dynamics and large atmospheric features.

6 DISCUSSION

In this section, we identify four qualitative circulation regimes in our parameter space and discuss their observational features. The regimes are characterized by different feature sizes, phase curve amplitudes, and zonal wind velocities.

6.1 Regime diagram

We can extract specific dimensional quantities from our simulations and plot them as functions of the non-dimensional parameters. The left-hand panel of Fig. 6 shows the size of the energy-containing wavelength of each simulation in our parameter space (Schneider & Walker 2006) calculated from the eddy kinetic energy spectrum (Read et al. 2018). This quantifies the size of the dominant features in Fig. 1 from their kinetic energy, confirming that simulations with large $\mathrm{Ro_T}$ or long $\hat{\tau}_{\mathrm{rad}}$ have large features with sizes on the order of 10°, while simulations with small $\mathrm{Ro_T}$ or short $\hat{\tau}_{\mathrm{rad}}$ have small features of the order of 1°. Short $\hat{\tau}_{\mathrm{rad}}$ strongly damps large features towards equilibrium, leaving only the recent localized small-scale forcing. Small $\mathrm{Ro_T}$ leads to weaker large-scale features due to its effect on the Rhines scale, as discussed in Section 4.2.

The left-hand panel of Fig. 6 shows the fractional amplitude (amplitude divided by mean value) of the phase curve in each simulation. Simulations with low $\mathrm{Ro_T}$ and high $\hat{\tau}_{\mathrm{rad}}$ have phase curves with high amplitudes, as they can support large-scale features that are not damped rapidly towards equilibrium. Note that these fractional amplitudes represent the maximum fractional amplitudes achievable by observations of the weather layer only; as discussed above, observations of near-infrared wavelengths may probe photospheres mostly below this layer. Observations of mid-infrared wavelengths with *JWST* may be able to measure thermal emission from photospheres that better correspond to our assumptions here.

These effects also govern the trends in zonal-mean zonal flow speed in Fig. 7. This shows the maximum zonal-mean zonal speed (east or west) of each simulation as a function of $\mathrm{Ro_T}$ and $\hat{\tau}_{\mathrm{rad}}$. The tests with high $\mathrm{Ro_T}$ can cascade energy up to larger scales and form zonal jets, but this process is suppressed for tests with low $\mathrm{Ro_T}$, as discussed previously. The tests with short $\hat{\tau}_{\mathrm{rad}}$ have weaker jets, again due to the rapid damping of perturbations back towards the uniform equilibrium geopotential field.

Fig. 8 is a schematic of the regimes that we identify based on all of our plots so far. Regime 1 has strong banded jets in both the east and west direction, as well as large vortices at various latitudes. This produces large variations in the phase curve and multiple peaks in the periodogram, broadening the main peak and even shifting it by large amounts away from the internal rotation rate. Regime 2 has strong westward equatorial jets and small vortices like the example in fig. 1A in Zhang & Showman (2014), and the similar regimes in Showman (2007), where strong zonal flow can only form on or near the equator.

Regime 3, with low $\mathrm{Ro_T}$, has no zonal jets and is dominated by the small-scale short-term forcing that we inject. Brown dwarfs in this regime would be characterized by constant-period phase curves, with properties determined by their radiative behaviour. This regime is like fig. 1B in Zhang & Showman (2014). Regime 4 is dominated by large-scale polar vortices produced by the injected vortices migrating to the poles and merging (Scott 2011). This circulation has little effect on the phase curves as the large polar vortices are centred on the axis of rotation.

6.2 Regime circulation

Figs 9, 10, 11, and 12 each show an example simulation from each regime in more detail. Regime 1 in Fig. 9 has strong banded zonal jets in both directions and has large planetary-scale vortices. It has a phase curve with a period shifted to longer periods than the rotation period by westward flowing height perturbations. As mentioned above, this shift corresponds to westward atmospheric motion of about 600 ms^{-1} at the equator or slower motion nearer the pole, according to equation (18). It has a weak half-period peak due to the variety of scales in its height perturbations. Its phase curve and periodogram are strongly affected by its atmospheric motion, and the dominant peak in its periodogram does not correspond to its actual rotation rate.

Regime 2 in Fig. 10 has a strong westward equatorial jet. This jet does not produce a notable shift in the periodogram like the L-dwarf does, because it is on the equator where the zonal temperature gradients are very small. Its phase curve and periodogram are mainly determined by the spatial frequencies in its height field. The strength of the half-period peak could be used to assess the length-scales of the average features.

Regime 3 in Fig. 11, with some possibility of large polar vortices if longer wavelength modes are excited as described in Zhang & Showman (2014). It has very small vortices due to its small geopotential. Its periodogram is centered on its rotation rate and is narrow. Its phase curve and periodogram do not depend strongly on its atmospheric dynamics, and the dominant period in its periodogram corresponds to its real rotation rate.

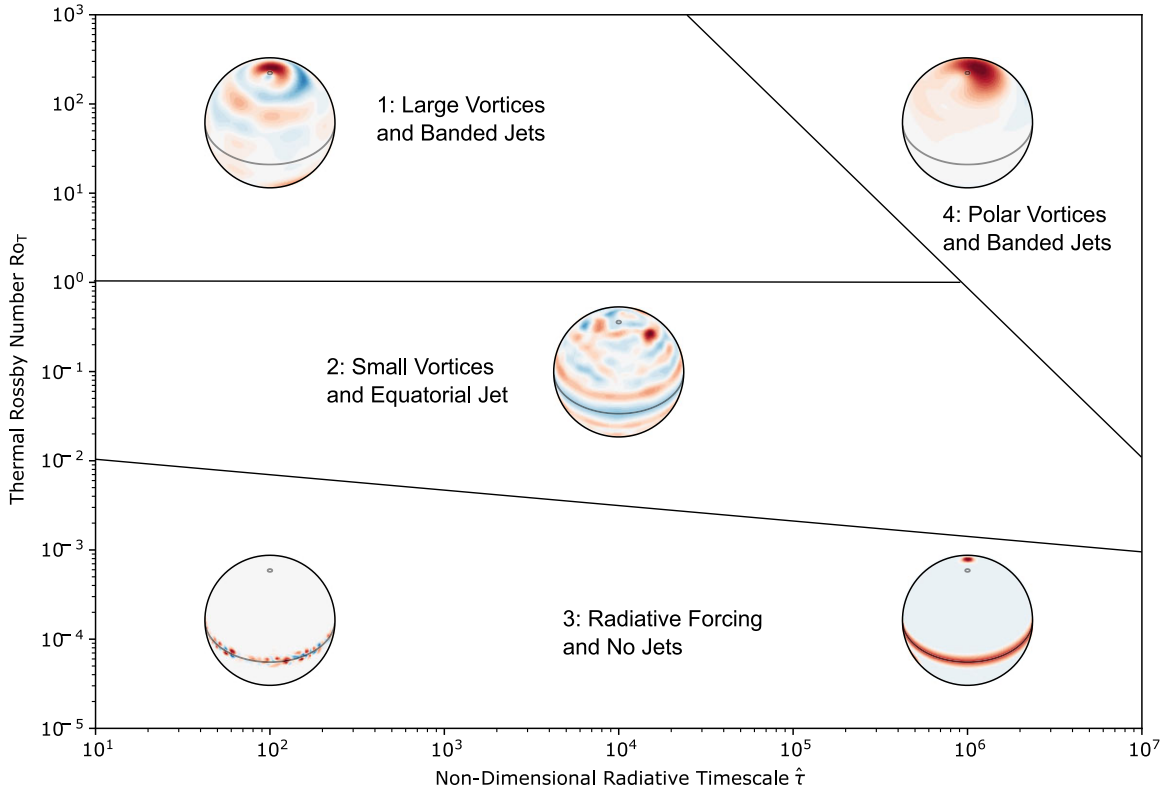

Figure 8. Schematic showing four circulation regimes that we identify qualitatively from our results. Orthographic plots of the geopotential fields in Fig. 1 are shown for several of the simulations, with the equator shown as a line and the pole marked as a point.

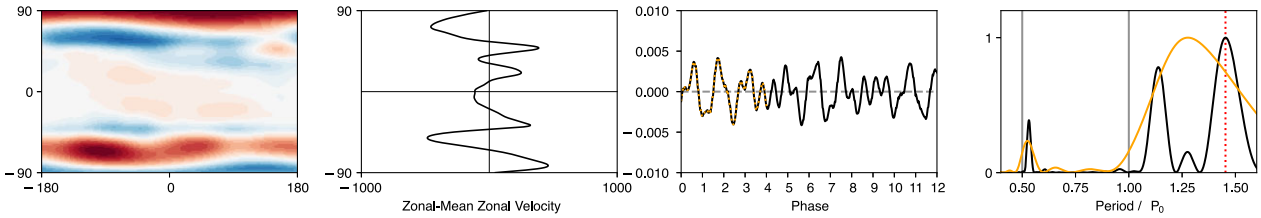

Figure 9. Example of 'Regime 1' with $Ro_T = 10^1$ and $\hat{\tau}_{rad} = 10^3$. From left to right, the plots show the instantaneous height field, instantaneous zonal-mean zonal velocity field, phase curve over 13.75 rotations, and periodogram for 13.75 rotations (black line) and 4 rotations (orange line).

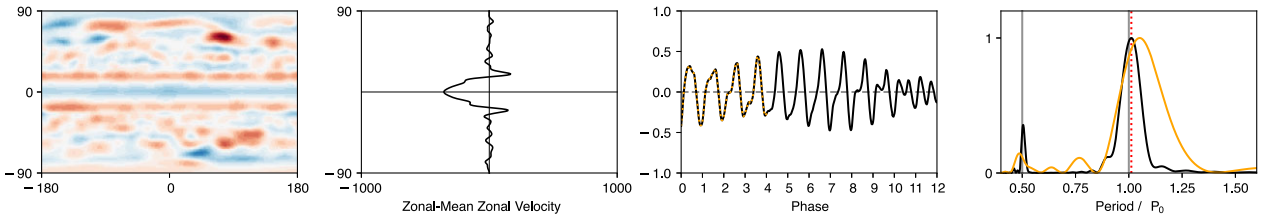

Figure 10. Example of 'Regime 2' with $Ro_T = 10^2$ and $\hat{\tau}_{rad} = 10^4$. From left to right, the plots show the instantaneous height field, instantaneous zonal-mean zonal velocity field, phase curve over 13.75 rotations, and periodogram for 13.75 rotations (black line) and 4 rotations (orange line).

Regime 4 in Fig. 11, with some possibility of large polar vortices if longer wavelength modes are excited as described in Zhang & Showman (2014). It has very small vortices due to its small geopotential. Its periodogram is centered on its rotation rate and is narrow. Its phase curve and periodogram do not depend strongly on its atmospheric dynamics, and the dominant period in its periodogram corresponds to its real rotation rate.

In each of Figs 9, 10, 11, and 12 we show periodograms calculated with different numbers of rotations to demonstrate potential issues with drawing observational conclusions from small numbers of rotations. The black periodogram lines were calculated using 13.75 rotations as shown in the adjacent phase curve. The orange periodogram lines were calculated using 4 rotations, shown as an orange-dashed line in the adjacent phase curve. The orange lines are notably broader and have different peak locations. This shows how a few

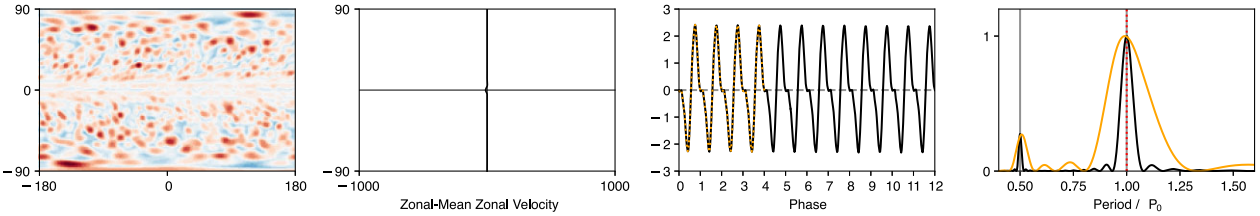

Figure 11. Example of 'Regime 3', with $\mathrm{Ro_T} = 10^{-3}$ and $\hat{\tau}_{\mathrm{rad}} = 10^{5}$. From left to right, the plots show the instantaneous height field, instantaneous zonal-mean zonal velocity field, phase curve over 13.75 rotations, and periodogram for 13.75 rotations (black line) and 4 rotations (orange line).

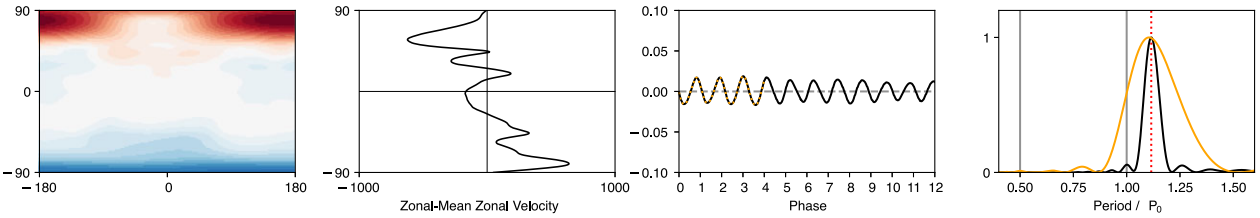

Figure 12. Example of 'Regime 4', with $\mathrm{Ro_T} = 10^{-3}$ and $\hat{\tau}_{\mathrm{rad}} = 10^{6}$. From left to right, the plots show the instantaneous height field, instantaneous zonal-mean zonal velocity field, phase curve over 13.75 rotations, and periodogram for 13.75 rotations (black line) and 4 rotations (orange line).

rotations may not be enough to accurately capture the atmospheric rotation rate or the structure of banded jets on brown dwarfs, given that deviations from the rotation period due to atmospheric motion may only produce changes in the infrared phase curve period of a few per cent.

We therefore urge caution about interpreting broad peaks as evidence for banded jets. If the spread of periods suggested by Apai et al. (2017) were to correspond to banded jets, this would imply very strong velocities and velocity gradients. For example, the spread of periods in their periodogram for their most rapidly rotating brown dwarf implies eastward and westward velocities of order 10 000 $\mathrm{ms^{-1}}$, which seems unrealistic in the light of the models in our study and other studies like Zhang & Showman (2014) and Tan & Showman (2021a). For relatively short periods of observation, it is possible that broad peaks are due to limited information like in Figs 9, 10, 11, and 12.

In general, we suggest that cooler brown dwarfs are likelier to support the regimes with high $\hat{\tau}_{\mathrm{rad}}$, and hotter brown dwarfs are likelier to support the regimes with low $\hat{\tau}_{\mathrm{rad}}$. This would lead us to expect Y-dwarfs to have circulation patterns related to zonal jets and polar vortices, L-dwarfs to have circulation patterns related to large-scale mid-latitude vortices, and T-dwarfs a mixture of both patterns.

However, each of these regimes could occur on each of the different spectral types of brown dwarf, due to their variety of parameters and the simplifications we have made here. The equilibrium geopotential parameter is especially uncertain, as a real 3D atmosphere can support vertical modes of different wavelengths corresponding to different deformation radii (Zhang & Showman 2014). Therefore, each spectral type could correspond to a range of values of $\mathrm{Ro_T}$ and so a large range of circulation regimes. Overall, these regimes should be interpreted as an idealized representation of the non-dimensional circulation patterns that are possible. It will be more useful to match them to observational results rather than to use them to predict observational results.

7 CONCLUSIONS

Observations of brown dwarfs show different types of variability, which can be fitted with different atmospheric features. We set out to model the entire parameter space of an idealized 2D model of a brown dwarf atmosphere, to describe its large-scale circulation regimes. We aim for the regimes in this model to be useful for interpreting time-resolved observations that need to be fitted with atmospheric circulation features. These idealized results could be used to guide more computationally expensive models that represent three dimensions or include more realistic physics.

By non-dimensionalizing our model, we reduced its large input parameter space to two non-dimensional parameters – the thermal Rossby number $\mathrm{Ro_T}$ and the non-dimensional radiative time-scale $\hat{\tau}_{\mathrm{rad}}$. We ran simulations covering the possible parameter space of these variables, defined by dimensional brown dwarf properties. These revealed distinctive circulation regimes, as summarized in Fig. 8:

(i) Regime 1 (high $\mathrm{Ro_T}$), with planetary-scale, zonally homogeneous features and strong banded zonal-mean zonal jets.

(ii) Regime 2 (intermediate $\mathrm{Ro_T}$), with medium-scale vortices and strong westward equatorial jets.

(iii) Regime 3 (low $\mathrm{Ro_T}$), with small-scale vortices determined primarily by the radiative forcing and almost no large-scale atmospheric dynamics.

(iv) Regime 4 (high $\mathrm{Ro_T}$ and high $\hat{\tau}_{\mathrm{rad}}$), dominated by polar vortices and highly zonally uniform features.

These produced different time-resolved observations, with the periods of phase curves shifted by zonal jets and broadened by banded jets. Different regimes contained half-period peaks of varying strength, produced by smaller scale features. The uncertainty in the model parameters makes it difficult to predictively link these regimes to specific types of brown dwarf. As they should define the entire range of possible behaviour in the potential parameter space, we suggest they could be useful for providing fittable features and classification regimes for observational results.

We also showed that single large polar vortices, similar to those on planets in the Solar system, can be present in brown dwarfs with a large geopotential or a low rotation rate. These could be important for the chemical or cloud composition of the objects, but would not greatly affect their phase curves themselves due to their polar position.

Our conclusions in relation to previous observations with *Spitzer* and *HST* were limited by the fact that these may have measured thermal emission partially or entirely from pressures deeper than the expected location of our simulated weather layer. The observed variability in these phase curves implies some effect from a weather layer with large-scale dynamics, but time-series observations with the MIRI instrument on *JWST* will ultimately be required to measure the relevant lower pressures directly.

We hope that this is a useful reference for observational studies, to understand which atmospheric features are plausible on different types of brown dwarf. Future work with the same model could look at the formation mechanism for the jets, waves, and vortices in more detail. It would also be useful to explore the effect of other parameters like the strength, spatial scale, and time-scale of the forcing, and to represent this in a less idealized way. More complex models with three dimensions, or including the effect of clouds, would be needed to simulate accurate observations for comparison with real data. Future observations to test these regimes would benefit from a high time resolution and a long observing period to resolve a high-resolution periodogram.

ACKNOWLEDGEMENTS

MH gratefully acknowledges funding from Christ Church, Oxford. This work was partly supported by a Science and Technology Facilities Council Consolidated Grant (ST/R000395/1), the Leverhulme Trust through a research project grant (RPG-2020-82) and a UKRI Future Leaders Fellowship (MR/T040866/1).

DATA AVAILABILITY

The original shallow-water model is available from gfdl.noaa.gov/idealized-spectral-models-quickstart. Simulation data is available on request to the corresponding author.

REFERENCES

Adams A. D., Millholland S., Laughlin G. P., 2019, AJ, 158, 108
Allers K. N., Vos J. M., Biller B. A., Williams P. K., 2020, Science, 368, 169
Apai D. et al., 2017, Science, 357, 683
Apai D., Nardiello D., Bedin L. R., 2021, ApJ, 906, 64
Artigau É., 2018, Variability of Brown Dwarfs. Springer International Publishing, Cham. p. 555
Artigau É., Bouchard S., Doyon R., Lafrenière D., 2009, ApJ, 701, 1534
Biller B., 2017, Astron. Rev., 13, 1
Brueshaber S. R., Sayanagi K. M., 2021, Icarus, 361, 114386
Brueshaber S. R., Sayanagi K. M., Dowling T. E., 2019, Icarus, 323, 46
Burningham B., Marley M. S., Line M. R., Lupu R., Visscher C., Morley C. V., Saumon D., Freedman R., 2017, MNRAS, 470, 1177
Burrows A., Hubbard W., Lunine J., Liebert J., 2001, Rev. Mod. Phys., 73, 719
Burrows A., Sudarsky D., Hubeny I., 2006, ApJ, 640, 1063
Cai T., Chan K. L., Mayr H. G., 2021, Planet. Sci. J., 2, 81
Cho J. Y.-K., Polvani L. M., 1996, Phys. Fluids, 8, 1531
Crossfield I. et al., 2014, Nature, 505, 654
Dawson A., 2016, J. Open Res. Softw., 4, 1
Galperin B., Read P. L., 2019, Zonal Jets: Phenomenology, Genesis, and Physics. Cambridge Univ. Press, Cambridge
Gordon C. T., Stern W. F., 1982, Mon. Weather Rev., 110, 625
Lee G. K., Casewell S. L., Chubb K. L., Hammond M., Tan X., Tsai S.-M., Pierrehumbert R. T., 2020, MNRAS, 496, 4674
Lomb N. R., 1976, Astrophys. Space Sci., 39, 447
Manjavacas E. et al., 2017, AJ, 155, 11
Mitchell J. L., Vallis G. K., 2010, J. Geophys. Res.: Planets, 115, E12
Mitchell D. M., Scott R. K., Seviour W. J., Thomson S. I., Waugh D. W., Teanby N. A., Ball E. R., 2021, Rev. Geophys., 59, e2020RG000723
Morley C. V., Marley M. S., Fortney J. J., Lupu R., Saumon D., Greene T., Lodders K., 2014a, ApJ, 787, 78
Morley C. V., Marley M. S., Fortney J. J., Lupu R., 2014b, ApJ, 789, L14
Phillips M. W. et al., 2020, A&A, 637, A38
Read P. L., Tabataba-Vakili F., Wang Y., Augier P., Lindborg E., Valeanu A., Young R. M., 2018, Q. J. R. Meteorol. Soc., 144, 2558
Reiners A., Basri G., 2008, ApJ, 684, 1390
Rhines P. B., 1975, J. Fluid Mech., 69, 417
Robinson T. D., Marley M. S., 2014, ApJ, 785, 158
Scargle J. D., 1982, ApJ, 263, 835
Schneider T., Walker C. C., 2006, J. Atmos. Sci., 63, 1569
Scott R., 2011, Geophys. Astrophys. Fluid Dyn., 105, 409
Scott R., Polvani L. M., 2007, J. Atmos. Sci., 64, 3158
Scott R., Polvani L. M., 2008, Geophys. Res. Lett., 35
Showman A. P., 2007, J. Atmos. Sci., 64, 3132
Showman A. P., Kaspi Y., 2013, ApJ, 776, 85
Showman A. P., Polvani L. M., 2011, ApJ, 738, 71
Showman A. P., Lewis N. K., Fortney J. J., 2015, ApJ, 801, 95
Showman A. P., Tan X., Zhang X., 2019, ApJ, 883, 4
Showman A. P., Tan X., Parmentier V., 2020, Space Sci. Rev., 216, 1
Simon A. A. et al., 2016, ApJ, 817, 162
Tan X., 2022, MNRAS, 511, 4861
Tan X., Showman A. P., 2019, ApJ, 874, 111
Tan X., Showman A. P., 2021a, MNRAS, 502, 2198
Tan X., Showman A. P., 2021b, MNRAS, 502, 678
Tang S.-Y., Robinson T. D., Marley M. S., Batalha N. E., Lupu R., Prato L., 2021, ApJ, 922, 26
Tremblin P., Amundsen D. S., Mourier P., Baraffe I., Chabrier G., Drummond B., Homeier D., Venot O., 2015, ApJ, 804, L17
Vallis G. K., 2006, Atmospheric and Oceanic Fluid Dynamics. Cambridge University Press, Cambridge, UK, p. 770
Vos J. M. et al., 2020, AJ, 160, 38
Vos J. M., Faherty J. K., Gagné J., Marley M., Metchev S., Gizis J., Rice E. L., Cruz K., 2022, ApJ, 924, 68
Wang Y., Read P. L., Tabataba-Vakili F., Young R. M., 2018, Q. J. R. Meteorolog. Soc., 144, 2537
Yang H. et al., 2016, ApJ, 826, 8
Zhang X., Showman A. P., 2014, ApJ, 788, L6
Zhou Y., Bowler B. P., Apai D., Kataria T., Morley C. V., Bryan M. L., Skemer A. J., Benneke B., 2022, AJ, 164, 239

This paper has been typeset from a TEX/LATEX file prepared by the author.